Continuum Differential Mechanisms and Their Applications in Gripper Designs

Kai Xu and Huan Liu

***Abstract*—Differential mechanisms possess various forms and are applied in a wide spectrum of mechanical systems. This paper proposes to categorize differential mechanisms into kinematic differential mechanisms (KDMs) and continuum differential mechanisms (CDMs), and also introduces two CDMs. The working principle, structures, constructions, and kinetostatic analyses of the proposed planar and the spatial CDMs are elaborated upon. The planar CDM is compared with two widely used differential mechanisms made from pulleys and linkages to show its effectiveness using a simple construction. The spatial CDM could resolve one input into three outputs in a way different from two serially connected planar differential mechanisms. As demonstrated in experimentation, the spatial CDM could allow more isotropic distribution of the three outputs. The categorization, analyses, and applications of the CDMs might not only extend the IFToMM terminology on differential mechanisms, but also inspire more CDM designs with distinct responses and properties for adaptive mechanical systems.**

***Index Terms*—Continuum mechanism, differential mechanism, force transmission matrix, gripper, kinetostatics.**

I. Introduction

According to the IFToMM terminology, a differential mechanism may resolve a single input into two outputs depending on the external constraints and loads [1]. Various differential mechanisms could be found in a wide spectrum of mechanical systems since the presence of a differential mechanism introduces a level of adaptivity and operation flexibility. For example, the differential mechanism in an automobile transmission allows the redistribution of the outputs, whereas the differential mechanisms in industrial grippers and robotic hands help form adaptive grasps.

Differential mechanisms usually possess several typical structures, including the following [2]:
1) pulley-based forms;
2) linkage-based forms;
3) gear-based forms;
4) fluidic T-pipe-based forms.

Since differential mechanisms are widely used, this study limits the literature review to their uses in gripping devices, such as robotic hands, industrial grippers, and prosthetic hands.

While used in multijoint industrial grippers or robotic hands, differential mechanisms reduce the number of actuators, reduce the control complexity, and form compliant and adaptive grasps. Then, various objects could be conveniently grasped by grippers and hands with a few actuators.

Moveable pulleys might be the most widely used design option to construct differential mechanisms. Using stacked moveable pulleys, multijoint prosthetic hands with one actuator were realized [3]–[5]. Linkage-based seesaw differential mechanisms are also used to achieve similar design goals, leading to designs of one-actuator humanoid robotic hands [6], [7]. What's more, differential mechanisms using planetary gears and fluidic T-shape pipes were also used, to design industrial grippers such as the SARAH-M1 hand [8] and the LIRMM hand [9].

It is possible to use differential mechanisms in a reversed way. Namely, two inputs are used to determine one output. For example, this approach has been applied to design prosthetic hands with mechanically implemented postural synergies, in which multiple sets of differential mechanisms are used to form grasping poses of a multijoint hand from two actuators. The examples include pulley-based designs [10]–[12] and planetary-gear-based designs [13], [14].

It is worth noting that using differential mechanisms is just one way to design underactuated grippers or hands. Other possibilities include the uses of spring-biased linkage [15], biased cable routing [16]–[19], biased gear transmission [20], and compliant structures [21]–[25].

Examining the mentioned differential mechanisms, one can conclude that three types could be categorized as kinematic differential mechanisms (KDMs):
1) the pulley-based designs;
2) the linkage-based designs;
3) the gear-based designs.

These KDMs generate differential outputs from the motions of the kinematic pairs. The fluidic T-pipe-based differential mechanism is not a KDM, since it generates differential outputs from the redistribution of its fluids.

This paper proposes to categorize differential mechanisms into KDMs and continuum differential mechanisms (CDMs). CDMs generate differential outputs via redistributions and/or deformations of their own materials and structures. The fluidic T-pipe-based differential mechanism could be referred to as a volume CDM, since its volume material is redistributed.

Two CDM designs are introduced: planar and spatial CDM, as shown in Fig. 1. Both CDMs generate differential outputs via deformations of their flexible structures. The working principle, constructions, kinetostatic analyses, and design examples are

Manuscript received December 23, 2015; revised April 11, 2016; accepted April 26, 2016. Date of publication May 20, 2016; date of current version June 3, 2016. This paper was recommended for publication by Associate Editor V. Krovi and Editor I.-M. Chen upon evaluation of the reviewers' comments. This work was supported by the National Program on Key Basic Research Projects under Grant 2011CB013300, in part by the Shanghai Rising-Star Program under Grant 14QA1402100, and in part by the National Natural Science Foundation of China under Grant 51435010 and Grant 51375295.

K. Xu is with the Laboratory of Robotics Innovation and Intervention, UM–SJTU Joint Institute, and with State Key Laboratory of Mechanical System and Vibration, Shanghai Jiao Tong University, Shanghai 200240, China (e-mail: k.xu@sjtu.edu.cn).

H. Liu is with the Laboratory of Robotics Innovation and Intervention, UM–SJTU Joint Institute, Shanghai Jiao Tong University, Shanghai 200240, China (e-mail: liuhuan_2013@sjtu.edu.cn).

Color versions of one or more of the figures in this paper are available online at http://ieeexplore.ieee.org.

Digital Object Identifier 10.1109/TRO.2016.2561295

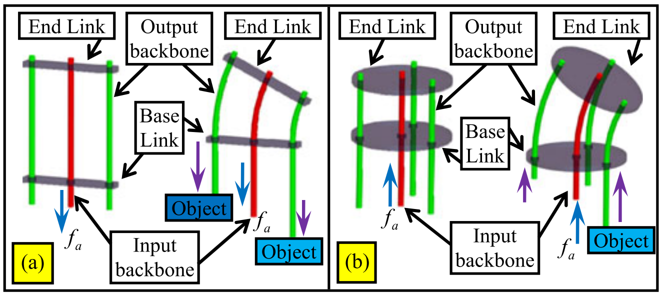

Fig. 1. Continuum differential mechanisms: (a) planar and (b) spatial forms.

presented. The planar CDM concept was proposed in a previous study [26], in which it was used to design a single-actuator prosthetic hand. The spatial CDM concept is proposed here for the first time.

Note that the proposed CDMs might be considered to be similar to parallel robots with flexible legs (e.g., the one in [27]). However, the essential working principle of a CDM is entirely different from the flexible-linked parallel robots.

The contributions of this paper include: 1) the proposal of the spatial CDM and the categorization for differential mechanisms; and 2) the kinetostatic analyses, comparisons, and experimental characterizations of two CDMs.

Exhibited by the designs and experimental results in [26] and later sections, major advantages of using CDMs include the design compactness and structure simplicity, besides the fact that a spatial CDM inherently resolves one input into three outputs. Due to the inherent compliance, the CDMs might not be suitable for the scenarios in which large output forces are needed. However, the CDMs could certainly find applications in which small differential output forces are needed in a confined space.

This paper is organized as follows. Section II presents the concept and working principle of the proposed CDMs. Section III presents detailed kinetostatic analyses and the comparisons of the CDMs with two other differential mechanisms. Design paradigms and the experimental characterizations are detailed in Section IV. The conclusion is summarized in Section V.

II. Continuum Differential Mechanisms

The proposed CDMs have planar and spatial forms, as shown in Fig. 1. They consist of a rigid base link, a flexible input backbone, a rigid end link, and two or three output backbones. The output backbones could be arranged arbitrarily around the input backbone in the spatial CDM, while the backbones are in a plane for the planar CDM. All the backbones are attached to the end link and can slide in holes in the base link.

The CDM can provide pushing as well as pulling outputs.

As shown in Fig. 1(a) for the planar CDM, a force f_a acts on the input backbone to generate two outputs to push external objects. When the load on the left is bigger (indicated by the longer arrow), continuing to drive the input backbone would bend all the backbones to generate differential outputs. The object on the right will be continuously pushed.

Similarly, in Fig. 1(b) for the spatial CDM, a force f_a on the input backbone could generate three pulling outputs (external objects are pulled). When the load on one backbone is bigger (indicated by the longer arrow), continuing to drive the input backbone would bend the spatial CDM for differential outputs.

The bent shapes of the backbones could be approximated as circular arcs according to previous analytical and experimental studies [28], [29]. A few spacer links might be needed between the end link and the base link for this assumption to hold, when the CDMs become relatively long. These backbones are not addressed as tendons because they can be pulled and pushed. A tendon usually can only be pulled.

The proposed CDMs generate differential outputs from the structure deformations. A fluidic T-pipe-based differential mechanism could be called a volume CDM to differentiate itself from the planar and spatial CDMs. The current IFToMM terminology on differential mechanisms actually only covers the KDM scenarios [1]. The CDMs could possibly resolve one input into multiple outputs. As shown in Section IV-B, the spatial CDM generates three outputs and the resolution is different from what is achieved by two serially connected planar CDMs. The spatial CDM could potentially allow more isotropic distribution of the outputs.

The proposed planar and spatial CDMs by no means exhaust the possibilities of other CDMs. Following the analyses and characterizations presented in this paper, one could also design other CDMs with different force transmission responses and properties for various adaptive mechanical systems.

III. Kinetostatic Analyses and Comparisons

This section presents kinetostatic analyses of the planar and spatial CDMs. Since the planar CDM resolves one input into two outputs, it is also compared to two widely used KDMs.

The CDMs generate differential outputs through their structure deformations. In order to unify and simplify the formulation of the kinetostatic analyses, the nomenclature is defined and the formulations are derived first for the spatial CDM. The planar CDM is then treated as a special case of the spatial CDM so that many symbol definitions could be shared.

A. Analysis of the Spatial Continuum Differential Mechanism

All the backbones of the spatial CDM could be pushed or pulled. As shown in Fig. 2(a), a force f_a on the input backbone generates three pushing outputs (external objects are pushed). When the external loads on f_2 and f_3 are bigger, continuous actuation of the input backbone will bend the spatial CDM. More pushing will be generated on the backbone of f_1. The shape of the spatial CDM varies with respect to different external resistances on the output backbones.

The backbones' bent shapes could be approximated as circular arcs [28], [29]. This assumption is fundamental to the presented kinetostatic analyses. Two coordinates are defined below with the nomenclature defined in Table I to describe the bent configuration of the spatial CDM: 1) Base link coordinate $\{b\} \equiv \{\hat{\mathbf{x}}_b, \hat{\mathbf{y}}_b, \hat{\mathbf{z}}_b\}$ is attached to the base link of the spatial CDM. The *XY* plane is aligned with the base link with its origin

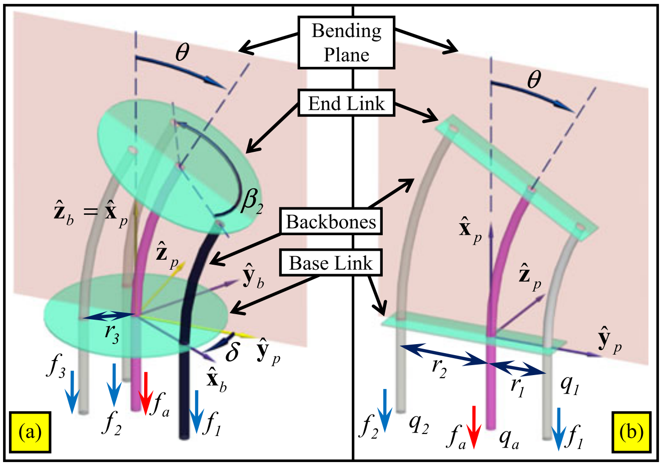

Fig. 2. Coordinates of the (a) spatial and (b) planar CDMs.

TABLE I
NOMENCLATURE USED IN THIS PAPER

Symbol	Definition
i	Index of the input and the output backbones, $i = a, 1, 2, 3$
r_i	Distance from the input backbone to the *i*th output backbone
β_i	Right-handed rotation angle from the *1*st to the *i*th output backbone; $\beta_1 = 0$ and β_i remain constant once the CDM is built.
l_i	Length of the *i*th backbone measured from the base link to the end link along the backbones
l_o	Original length of the backbones when the CDM is in its initial straight configuration
q_i	Translation distance of the *i*th backbone; $q_i \equiv l_i - l_o$
f_i	Input or output force of the *i*th backbone
E_i	Young's modulus of the *i*th backbone
I_i	Cross section area moment of inertia of the *i*th backbone
ρ_i	Radius of curvature of the *i*th backbone
δ_i	A right-handed rotation angle about $\hat{\mathbf{z}}_b$ from $\hat{\mathbf{y}}_p$ to a ray passing through the input backbone and the *i*th output backbone.
δ	$\delta \equiv \delta_1$ and $\delta_i = \delta + \beta_i$
$\theta(s)$	The angle of the tangent to the input backbone along its length in the bending plane. Under the constant curvature assumption, this angle at the tip of the input backbone is more of concern and it is designated as θ.
Ω_p, Ω_s	Potential energy of the planar and the spatial CDMs

at the link's center. $\hat{\mathbf{x}}_b$ points from the center to the first output backbone. The output backbones are numbered according to the definition of δ_i. 2) Bending plane coordinate $\{p\} \equiv \{\hat{\mathbf{x}}_p, \hat{\mathbf{y}}_p, \hat{\mathbf{z}}_p\}$ shares its origin with $\{b\}$ and has the CDM bent in its *XY* plane.

When the spatial CDM is used, the position and orientation of the end link are usually not of direct concern. Otherwise, more coordinates will be needed to fully describe its shape.

The spatial CDM is a three-degree-of-freedom (DoF) system such that it resolves one input into three outputs. Its configuration could be described by either of two sets of variables: q_a, θ, and δ or q_1, q_2, and q_3.

Under the circular bending assumption as in [28] and [29], the output backbones are bent into circular arcs in planes parallel to the bending plane. The projection of the *i*th output backbone on the bending plane has the same length as the output backbone itself. The projection of the output backbone is offset from the input backbone within the bending plane. The radius of the projected output backbone is related to the radius of the input backbone as in (1). The arrangement of the output backbones could be arbitrary by assigning different values to r_i and β_i as

$$\rho_a = \rho_i + r_i \cos\delta_i = \rho_i + r_i \cos(\delta + \beta_i). \tag{1}$$

The lengths of the input backbone and the *i*th output backbone are then related according to (2), which leads to (3) following the definition of q_i in Table I as

$$l_a = \rho_a \theta = \rho_i \theta + r_i \theta \cos(\delta + \beta_i) = l_i + r_i \theta \cos(\delta + \beta_i) \tag{2}$$

$$q_i = q_a - r_i \theta \cos(\delta + \beta_i). \tag{3}$$

The input and output forces of the spatial CDM could be related using the virtual work principle as in (4) with the matrix form as in (5). In (4), the work done by the input forces toward the CDM is equal to the sum of the work done by the CDM and the increment of the CDM's internal energy

$$f_a \Delta q_a = f_1 \Delta q_1 + f_2 \Delta q_2 + f_3 \Delta q_3 + \Delta\Omega_s \tag{4}$$

$$\begin{bmatrix} f_a & 0 & 0 \end{bmatrix} \begin{bmatrix} \Delta q_a \\ \Delta\theta \\ \Delta\delta \end{bmatrix} - \nabla\Omega_s^T \begin{bmatrix} \Delta q_a \\ \Delta\theta \\ \Delta\delta \end{bmatrix} = \begin{bmatrix} f_1 & f_2 & f_3 \end{bmatrix} \begin{bmatrix} \Delta q_1 \\ \Delta q_2 \\ \Delta q_3 \end{bmatrix} \tag{5}$$

where $\nabla\Omega_s = [\partial\Omega_s/\partial q_a \;\; \partial\Omega_s/\partial\theta \;\; \partial\Omega_s/\partial\delta]^T$ is the gradient.

Equation (6) could be obtained by differentiating (3) with respect to q_a, θ, and δ as

$$\begin{bmatrix} \Delta q_1 & \Delta q_2 & \Delta q_3 \end{bmatrix}^T = \mathbf{J}_{3q} \begin{bmatrix} \Delta q_a & \Delta\theta & \Delta\delta \end{bmatrix}^T \tag{6}$$

where

$$\mathbf{J}_{3q} = \begin{bmatrix} 1 & -r_1 \cos\delta & r_1\,\theta \sin\delta \\ 1 & -r_2 \cos\delta_2 & r_2\,\theta \sin\delta_2 \\ 1 & -r_3 \cos\delta_3 & r_3\,\theta \sin\delta_3 \end{bmatrix}.$$

The output forces f_i could be calculated as in (7), with (6) substituted into (5). Hence, $\boldsymbol{T}_{3c}$ in (8) is the transmission matrix for the spatial CDM as

$$\begin{bmatrix} f_1 \\ f_2 \\ f_3 \end{bmatrix} = \left(\mathbf{J}_{3q}^T\right)^{-1} \left(\begin{bmatrix} f_a \\ 0 \\ 0 \end{bmatrix} - \nabla\Omega_s \right) = \mathbf{T}_{3c} \begin{bmatrix} f_a \\ -\nabla\Omega_s \end{bmatrix} \tag{7}$$

$$\mathbf{T}_{3c} = \left(\mathbf{J}_{3q}^T\right)^{-1} \begin{bmatrix} 1 & 1 & 0 & 0 \\ 0 & 0 & 1 & 0 \\ 0 & 0 & 0 & 1 \end{bmatrix}. \tag{8}$$

Gravity is neglected in the existing study for the analyses of differential mechanisms [2]. In order to keep the derivations and comparisons consistent, gravity is also neglected in the expression of Ω_s. Following the circular bending assumption, the CDM's potential energy could be written as in (9) with the

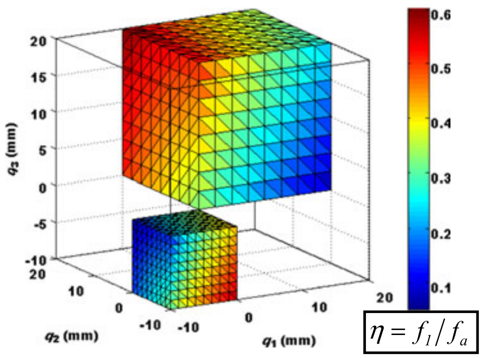

Fig. 3. Visualization of the force transmission property of the spatial CDM.

TABLE II
STRUCTURAL PARAMETERS OF THE DIFFERENTIAL MECHANISMS

Spatial CDM		$\beta_2 = 2\pi/3$	$\beta_3 = 4\pi/3$
$l_o = 20$ mm	$r_i = 30$ mm	$E_i = 50$ GPa	$I_i = 0.1018\,\mathrm{mm}^4$
Planar CDM		Pulley differential mechanism	
$l_o = 20$ mm	$E_i = 50$ GPa	$r_1 = 30$ mm	$r_2 = 30$ mm
$r_i = 30$ mm	$I_i = 0.1018\,\mathrm{mm}^4$	$K_1 = 0$ N/m	$K_2 = 0.4$ N·m/rad
Seesaw differential mechanism		$r_1 = 30$ mm	$r_2 = 30$ mm
$l_o = 20$ mm	$b_i = 60$ mm	$K_1 = 0$ N/m	$K_2 = 0.4$ N·m/rad

gradient as

$$\Omega_s = \frac{E_a I_a \theta^2}{2l_a} + \frac{E_1 I_1 \theta^2}{2l_1} + \frac{E_2 I_2 \theta^2}{2l_2} + \frac{E_3 I_3 \theta^2}{2l_3} \tag{9}$$

$$\nabla\Omega_s = \begin{bmatrix} -\frac{E_a I_a \theta^2}{2l_a^2} - \sum_{i=1}^{3} \frac{E_i I_i \theta^2}{2l_i^2} \\ \frac{E_a I_a \theta}{l_a} + \sum_{i=1}^{3} \frac{E_i I_i \theta}{l_i} + \sum_{i=1}^{3} \frac{E_i I_i \theta^2 r_i \cos\delta_i}{2l_i^2} \\ -\frac{\theta^3}{2} \sum_{i=1}^{3} \frac{E_i I_i r_i \sin\delta_i}{l_i^2} \end{bmatrix}. \tag{10}$$

A plot could be generated to visualize the force transmission property of the spatial CDM, as in Fig. 3. The structural parameters are listed in Table II. The cross-sectional area moment of inertia is calculated for a backbone with a round cross section and a diameter of 1.2 mm.

In Fig. 3, the points are distributed on two cubes with the edge lengths of 20 and 10 mm, respectively. The coordinates of the points correspond to the actuation lengths q_1, q_2, and q_3.

The CDM is an underactuated structure. When $f_a > 0$ (upward) $q_i > 0$ (the CDM becomes longer). When $f_a < 0$ (downward) $q_i < 0$ (the CDM becomes shorter). The plot in Fig. 3 is, hence, generated only for $q_i > 0$ and $q_i < 0$.

Since the initial length l_o of the spatial CDM is 20 mm, as in Table II, and the CDM is shortened when $q_i < 0$, the condition of $q_i \geq -10$ mm is adopted to avoid excessive bending of the backbones. The input backbone is pushed and the CDM is lengthened when $q_i > 0$. The condition of $q_i \leq 20$ mm is adopted to avoid buckling of the input backbone.

For a specific set of q_1, q_2, and q_3, the corresponding q_a, θ, and δ are obtained according to (3). Then, the q_a, θ, and δ values are used to calculate the force transmission matrix as in (8) and the force outputs. The output force ratio $\eta = f_1/f_a$ is mapped to a color of each point in Fig. 3. The color map in Fig. 3 is set to ease the comparison to those in Fig. 6(b).

B. Analysis of the Planar Continuum Differential Mechanism

The planar CDM only bends in the bending plane. The symbol definitions are consistent with those of the spatial CDM. For the planar CDM, $\delta = 0$, $\beta_2 = \pi$, and $\theta \in [-\pi/2, \pi/2]$.

The planar CDM is a 2-DoF system and its configuration could be described by either of the two pairs of variables: q_a and θ, or q_1 and q_2. Simplifying (1) and (3) gives

$$\rho_a = \rho_1 + r_1 = \rho_2 - r_2 \tag{11}$$

$$q_1 = q_a - r_1\theta \text{ and } q_2 = q_a + r_2\theta. \tag{12}$$

Note that $q_i < 0$ when the CDM is shortened to generate pushing outputs, according to the definition of q_i in Table I. This definition is also consistent with the direction of $\hat{\mathbf{x}}_p$. In the configuration as in Fig. 2(b), q_i satisfies that $q_1 < q_a < q_2 < 0$.

The input and the output forces are again related using the virtual work principle as in (13) with the matrix form as in (14) as

$$f_a \Delta q_a = f_1 \Delta q_1 + f_2 \Delta q_2 + \Delta\Omega_p \tag{13}$$

$$\begin{bmatrix} f_a & 0 \end{bmatrix} \begin{bmatrix} \Delta q_a \\ \Delta\theta \end{bmatrix} - \nabla\Omega_p^T \begin{bmatrix} \Delta q_a \\ \Delta\theta \end{bmatrix} = \begin{bmatrix} f_1 & f_2 \end{bmatrix} \begin{bmatrix} \Delta q_1 \\ \Delta q_2 \end{bmatrix} \tag{14}$$

where $\nabla\Omega_p \in \Re^{2\times1} = [\partial\Omega_p/\partial q_a \;\; \partial\Omega_p/\partial\theta]^T$ is the gradient.

Differentiating (12) with respect to q_a and θ gives $\mathbf{J}_{2q}$

$$\begin{bmatrix} \Delta q_1 & \Delta q_2 \end{bmatrix}^T = \mathbf{J}_{2q} \begin{bmatrix} \Delta q_a & \Delta\theta \end{bmatrix}^T \tag{15}$$

where

$$\mathbf{J}_{2q} = \begin{bmatrix} \partial q_1/\partial q_a & \partial q_1/\partial\theta \\ \partial q_2/\partial q_a & \partial q_2/\partial\theta \end{bmatrix} = \begin{bmatrix} 1 & -r_1 \\ 1 & r_2 \end{bmatrix}.$$

The output forces f_i of the planar CDM are calculated as in (16), with (15) substituted into (14). $\mathbf{T}_{2c}$ is, hence, the transmission matrix for the planar CDM as

$$\begin{bmatrix} f_1 \\ f_2 \end{bmatrix} = \left(\mathbf{J}_{2q}^T\right)^{-1} \left(\begin{bmatrix} f_a \\ 0 \end{bmatrix} - \nabla\Omega_p \right) = \mathbf{T}_{2c} \begin{bmatrix} f_a \\ -\nabla\Omega_p \end{bmatrix} \tag{16}$$

$$\mathbf{T}_{2c} = \left(\mathbf{J}_{2q}^T\right)^{-1} \begin{bmatrix} 1 & 1 & 0 \\ 0 & 0 & 1 \end{bmatrix} = \frac{1}{r_1 + r_2} \begin{bmatrix} r_2 & r_2 & -1 \\ r_1 & r_1 & 1 \end{bmatrix}. \tag{17}$$

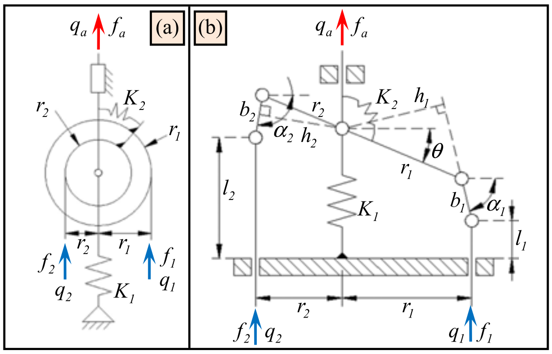

Fig. 4. Differential mechanisms. (a) Pulley-based mechanism. (b) Seesaw-linkage-based mechanism.

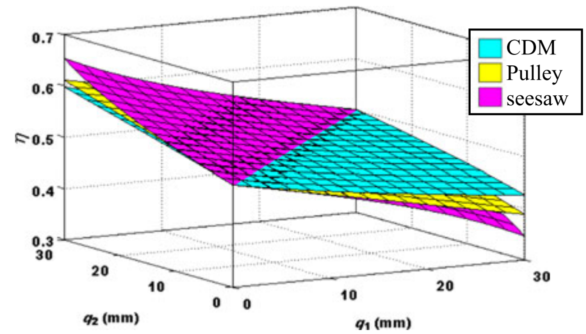

Fig. 5. Comparison of the force transmission property $\eta = f_1/f_a$ of the three differential mechanisms.

Gravity is neglected and the planar CDM's potential energy could be written as in (18) with the gradient as in (19) as

$$\Omega_p = \frac{E_a I_a \theta^2}{2l_a} + \frac{E_1 I_1 \theta^2}{2l_1} + \frac{E_2 I_2 \theta^2}{2l_2} \tag{18}$$

$$\nabla\Omega_p = \begin{bmatrix} -\frac{E_a I_a \theta^2}{2l_a^2} - \frac{E_1 I_1 \theta^2}{2l_1^2} - \frac{E_2 I_2 \theta^2}{2l_2^2} \\ \frac{E_a I_a \theta}{l_a} + \frac{E_1 I_1 \theta}{l_1} + \frac{E_2 I_2 \theta}{l_2} + \frac{E_1 I_1 \theta^2 r_1}{2l_1^2} - \frac{E_2 I_2 \theta^2 r_2}{2l_2^2} \end{bmatrix}. \tag{19}$$

C. Comparisons With Two Differential Mechanisms

The planar CDM resolves one input into two outputs, as do many existing differential mechanisms. The planar CDM is hence compared to two widely used KDMs: a pulley-based mechanism and a seesaw-linkage-based one.

When $q_i > 0$, the planar CDM becomes longer and generates pulling outputs. In order to keep the comparison consistent, the diagrams in Fig. 4 are, hence, defined so that pulling outputs correspond to $q_i > 0$.

A general form of the pulley differential mechanism is shown in Fig. 4(a). Cables for outputs are wound around two pulleys that are fixed together. A linear spring with stiffness K_1 and a torsional spring with a stiffness K_2 are added to constrain the pulley movements. The input force f_a acts on the pulley center to generate two outputs. These differential pulleys have been widely used (e.g., in the prosthetic hand designs [3], [19]).

The force transmission matrix $\mathbf{T}_p$ could be derived as follows according to the approaches in [2]. The positive q_a is indicated by the arrow in Fig. 4(a). The positive θ is defined as a left-handed rotation about the pulley center. In this way, $\theta > 0$ when $q_2 > q_1$. The sign of θ is, hence, consistent with that of the planar CDM as

$$\begin{bmatrix} f_1 \\ f_2 \end{bmatrix} = \mathbf{T}_p \begin{bmatrix} f_a \\ -K_1 q_a \\ -K_2\theta \end{bmatrix}, \quad \text{where } \mathbf{T}_p = \frac{1}{r_1 + r_2}\begin{bmatrix} r_2 & r_2 & -1 \\ r_1 & r_1 & 1 \end{bmatrix}. \tag{20}$$

q_a and θ are related to q_1 and q_2 as in (21). The signs of q_i are defined consistently with those in (12) as

$$q_1 = q_a - r_1\theta \text{ and } q_2 = q_a + r_2\theta. \tag{21}$$

The seesaw differential mechanism is shown in Fig. 4(b). The input force f_a acts on a pivot point. When the external loads are not balanced, the lever will be tilted and differential outputs will be generated. This seesaw differential mechanisms are also often used (e.g., in the hand designs in [4], [6], and [7]).

The level tilting angle is characterized by θ and its positive value is defined as a left-handed rotation about the center for the same reason mentioned before. The positive q_a is indicated by the arrow in Fig. 4(b). With other entities defined as in Fig. 4(b), the transmission matrix $\mathbf{T}_s$ could be derived as follows according to the approaches in [2]:

$$\begin{bmatrix} f_1 \\ f_2 \end{bmatrix} = \mathbf{T}_s \begin{bmatrix} f_a \\ -K_1 q_a \\ -K_2\theta \end{bmatrix} \tag{22}$$

where

$$\mathbf{T}_s = \frac{1}{h_1' + h_2'}\begin{bmatrix} h_2' & h_2' & -1 \\ h_1' & h_1' & 1 \end{bmatrix}, \quad h_1' = \frac{h_1}{\sin\alpha_1},$$

and $$h_2' = \frac{h_2}{\sin\alpha_2}.$$

In a practical setting, the two springs K_1 and K_2 in the pulley and the seesaw differential mechanisms usually are not installed. The inclusion of the two springs is to demonstrate the equivalency between the pulley/seesaw differentials and the planar CDM. It could be observed that the two items in $\nabla\Omega_{\mathrm{p}}$ have the physical meanings of the two springs, which try to affect the motions of the planar CDM.

With the force transmission matrices ($\mathbf{T}_{2c}$, $\mathbf{T}_p$, and $\mathbf{T}_s$), the properties of the force transmission of the planar CDM, the pulley, and the seesaw differential mechanisms could be visualized and compared as in Fig. 5.

The plots in Fig. 5 are generated with respect to the actuation lengths q_1 and q_2. Since the pulley differential can only generate pulling outputs, the plot is only generated for positive q_i to facilitate the comparison. For a specific pair of q_1 and q_2, the corresponding q_a and θ are obtained according to (12) to calculate the force transmission matrix and the force outputs. The plots in Fig. 5 depict the output force ratio $\eta = f_1/f_a$ for the differential mechanisms.

All of the structural parameters are listed in Table II. The cross-sectional area moment of inertia is from a $\varnothing 1.2$-mm backbone.

For the pulley differential mechanism, the radii of the pulleys are set to the same values as r_i of the planar CDM. The stiffness K_1 and K_2 will be determined. Since the plots are generated for $q_i \in [0, 30\text{ mm}]$, setting $q_a = 15$ mm leads to the approximation that $l_a = l_1 = l_2 = 35$ mm. With $r_1 = r_2$, comparing $-K_2\theta$ in (20) to the corresponding part in (16) gives an approximated value of $K_2 = 0.436$ N·m/rad according to (23). K_2 is, hence, set to 0.4 N·m/rad, as in Table II. K_1 could be estimated by comparing $-K_1 q_a$ in (20) to the corresponding part in (16) according to (23). $q_i \in [0,\ 30\text{ mm}]$ gives $\theta \in [0,\ 0.50\text{ rad}]$. Using $\theta = 0.25$ rad and $l_a = l_1 = l_2 = 35$ mm, the calculation would estimate K_1 to be about -26.0 N/m.

Particular attentions should be paid to this equivalent stiffness K_1 of a negative value. The explanation is as follows. When the planar CDM is extended and bent, its internal energy is released when it is further extended with the same amount of bending. Namely, increasing q_a corresponds to a decrease of its internal energy. This behavior is like a spring with negative stiffness. On the contrary, increasing q_a would increase the internal energy in the pulley and the seesaw differential mechanisms in which $K_1 > 0$. Since it is not practical to include a spring with a negative stiffness, K_1 is set to 0 N/m in Table II

$$K_1 \approx \frac{1}{q_a}\frac{\partial \Omega_p}{\partial q_a} \quad \text{and} \quad K_2 \approx \frac{1}{\theta}\frac{\partial \Omega_p}{\partial \theta}. \tag{23}$$

For the seesaw differential mechanism, r_1, r_2, K_1, and K_2 are set to the same values as the pulley differential mechanism. The link lengths b_1 and b_2 are set to a relatively large value (e.g., 60 mm, as in Table II) so that the α_1 and α_2 angles are close to 90°. Otherwise, the outputs could become highly nonlinear.

It could be observed from Fig. 5 that the differential outputs realized by a planar CDM are very similar to those by a pulley or a seesaw different mechanism. The planar CDM intrinsically adds two "virtual" springs upon the outputs, which are reflected by the two terms in its energy gradient. One virtual spring is equivalent to K_1, affecting the overall outputs. The other is equivalent to K_2, balancing the two outputs.

Sophisticated optimizations could certainly be formulated to generate better structural parameters of r_i, b_i, K_1, and K_2 for the pulley and the seesaw differential mechanisms so that the plots in Fig. 5 could become even more similar. The current parameters are considered to be accurate enough to demonstrate the equivalency between the planar CDM and the pulley/seesaw differential mechanisms.

Both the planar and spatial CDMs could be stacked to form a multistage CDM. The force transmission matrix can be derived following the general approach presented in [2].

IV. Gripper Designs and Experimentation

Experimental quantifications of the force transmission properties of the planar and the spatial CDMs are first presented in Section IV-A to further demonstrate their features. Then, a gripper design example and its experimental characterizations are presented in Section IV-B, particularly revealing the differences between a spatial CDM and two serially stacked planar CDMs.

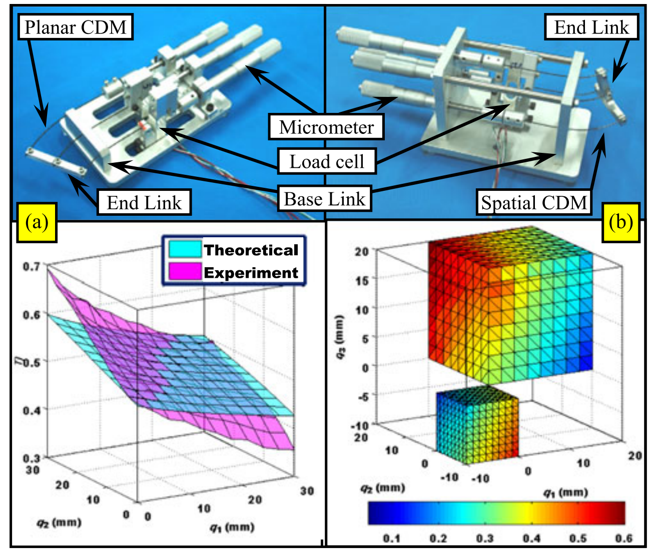

Fig. 6. Quantification of the force transmission properties of (a) the planar CDM and (b) the spatial CDM: experimental setup and measurement results.

A. Force Transmission Properties of the Continuum Differential Mechanisms

The force transmission properties are of great importance for any differential mechanisms. Experimental quantifications of the force transmission properties of the planar and the spatial CDMs were carried out. The experimental setups for the planar and the spatial CDMs are shown in Fig. 6.

Structural parameters of this planar CDM are listed in Table II. For a specific pair of q_1 and q_2 values, the q_a value was calculated according to (12). Three micrometers were used to push and pull the input and the output backbones so that the backbones' desired actuation lengths are reached, as shown in Fig. 6(a). These micrometers were rated for a 200-N load with an accuracy of 0.01 mm.

Then, the q_a micrometer continued to actuate the input backbone until a 30-N input force f_a was created. The output force f_1 was read and the ratio $\eta = f_1/f_a$ was recorded. The forces were measured using two bending-beam-type load cells (YZC-133, from Guangzhou Measurement Inc., China, with a measurement range of ±50 N). Connection accessories were made and assembled to the load cells to ensure a proper loading condition. Voltage outputs from the load cells were measured using an A/D card (PCL-818HG from AdvanTech Inc. with a 12-bit conversion resolution and an adjustable gain up to 1000). The measurement results are plotted as in Fig. 6(a). The theoretical results are also plotted for comparison.

The experiments for quantifying the spatial CDM's force transmission properties were carried out similarly. Structural parameters of this spatial CDM are also listed in Table II. The end link was made to a *Y* shape to reduce the weight. For a set of q_1, q_2, and q_3, the q_a value was calculated according to (3). Four micrometers were used to push and pull the input and the output backbones so that the backbones' desired actuation lengths are reached. Then, the q_a micrometer continued to actuate the input backbone until a 30-N input force f_a was reached. The output

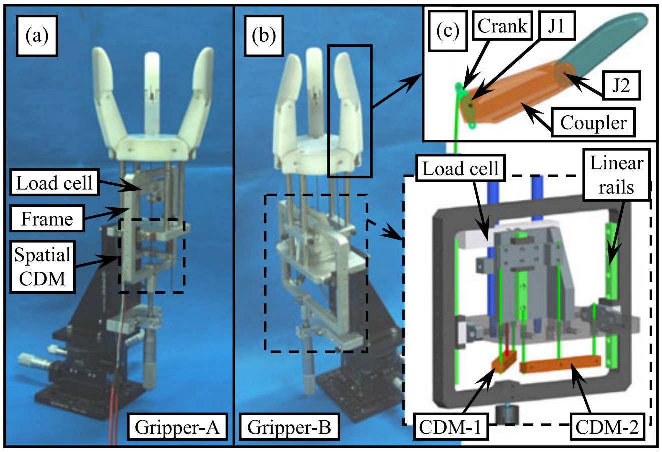

Fig. 7. Three-fingered grippers actuated by (a) spatial CDM and (b) two serially connected planar CDMs.

force f_1 was read and the ratio $\eta = f_1/f_a$ was recorded. The measurement results are plotted as in Fig. 6(b) for the comparison to the theoretical results in Fig. 3.

From the experimental results in Fig. 6, it could be seen that the discrepancy between the theoretic force ratio η and the actual value varies from –0.10 to 0.10. Several reasons could contributed to the discrepancy, such as uncertainties in the material properties and fabrication tolerances. In the CDMs' kinetostatic analyses, the backbone shapes are assumed to be circular. This assumption is of less accuracy when the backbones are heavily pushed or pulled. In addition, this assumption would be further affected by gravity when the CDMs are longer (q_i increases). The discrepancy is bigger in Fig. 6 for bigger q_i. In order to maintain the force transmission properties in (7) and (16) to be accurate, two criteria should be followed if one tries to implement the spatial and the planar CDMs: 1) a CDM should be kept as short as possible to a point that plastic deformations do not occur and 2) the forces on the backbones should be kept reasonably below critical loadings for buckling. Otherwise, more accurate modeling of the backbones and calibrations of the CDM constructions might be needed to better describe the force transmission properties.

B. Gripper Performance Characterizations

The spatial CDM resolves one input into three outputs, while the planar CDM is essentially equivalent to the pulley or the linkage-based KDMs. A main advantage of using CDMs is the design's compactness and structural simplicity. This has been partially demonstrated by the single-actuator prosthetic hand design and its experimentation in [26].

This section further presents the design and experimentation of two three-fingered grippers actuated by a spatial CDM (Gripper-A) and two serially stacked planar CDMs (Gripper-B), as shown in Fig. 7. Hopefully, the grippers' simple construction would inspire more CDM-based mechanism designs.

The fingers in Gripper-A and Gripper-B are identical, as in Fig. 7(c). Lengths of the distal and proximal phalanges are 60 and 70 mm, respectively. Motions of the J1 and the J2 joints are

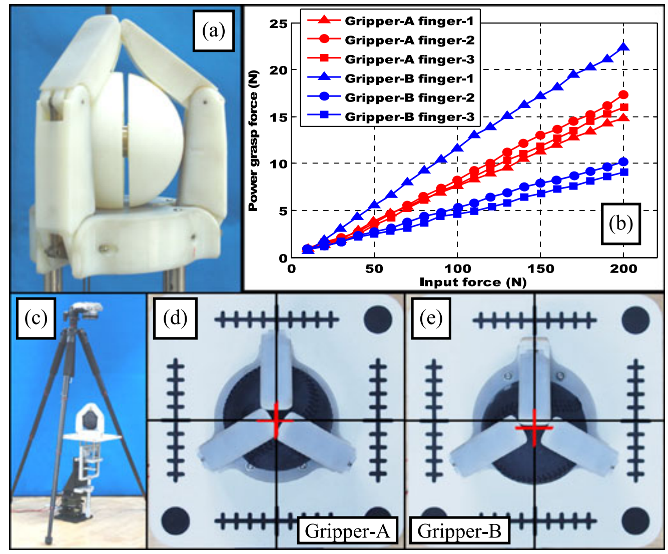

Fig. 8. Grasping experiments: (a) measure the grasping forces from different fingers, (b) measurement results, (c) the setup for grasping pose visualization, and (d) and (e) the grasping poses of Gripper-A and Gripper-B.

coupled through a coupler. A torsional spring is installed at the J2 joint. When the crank is rotated by pulling the output backbone, the J1 joint will rotate first. Then, if the proximal phalange encounters an object, continuous pulling of the backbone will close the J2 joint.

The Gripper-A fingers are actuated by a spatial CDM. When the fingers encounter different external loads, continuous push of the input backbone will bend the spatial CDM so that the fingers will close adaptively.

In order to reveal the characteristics of the spatial CDM that resolves one input into three outputs, the Gripper-B fingers are actuated by two serially connected planar CDMs. One output backbone of the CDM-1 is connected to the input backbone of the CDM-2. The connection is guided by a linear rail.

The characterization experiments include grasping, pinching, and the pull-out experiments, referring to the examples in [30]. During the experiments, it was observed that buckling did not occur on any backbones.

Both grippers in Fig. 7 are actuated to manually provide a pushing input to the CDMs. Three pulling outputs were then generated to close the fingers. A load cell (YZC-135 from Guangzhou Measurement Inc., China, with a measurement range of ± 200 N) was used to monitor the input force. A frame guided by two linear rails was used in both grippers to ensure proper loading to the input backbone.

The grasping experiments were performed as shown in Fig. 8(a). One ATI Nano 17 6-D force sensor was installed inside a 3-D-printed ball with a diameter of 73 mm (a baseball size). The experiments were performed three times. Each time, one half of the ball was placed toward one finger to measure the grasping force generated by that finger. The results are plotted in Fig. 8(b) when the actuation force increases from 10 to 200 N. It could be easily seen that the Gripper-A fingers generate similar grasping forces, while one of the Gripper-B fingers generates higher forces than the other two. In order to further illustrate the

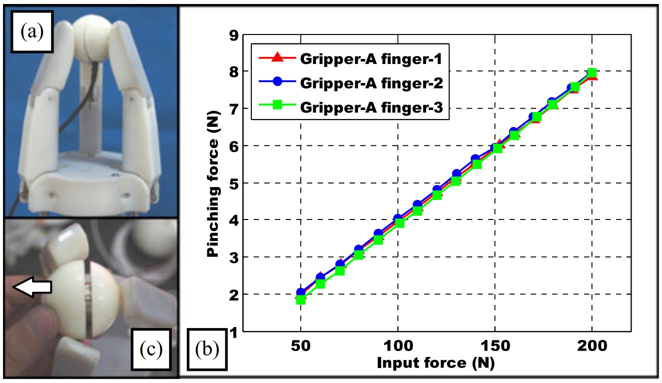

Fig. 9. Pinching experiments: (a) measure the pinching forces from different fingers, (b) measurement results, and (c) failed pinch on Gripper-B.

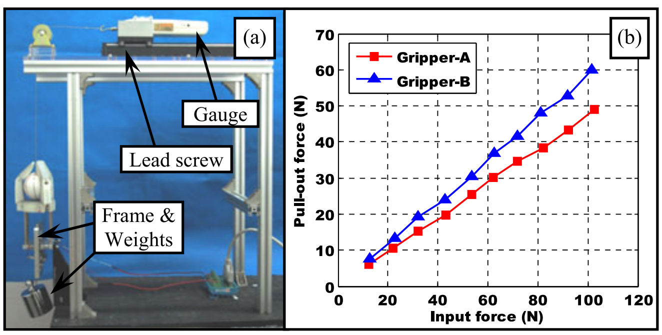

Fig. 10. Pull-out experiments. (a) Setup. (b) Measurement results.

difference, the grasping poses of the two grippers are visualized as in Fig. 8(c). The ball grasped is a baseball painted black for better visualization. It could be seen from Fig. 8(d) and (e) that Gripper-B pushes the ball aside due to the imbalanced outputs from the two serially connected planar CDMs.

The pinching experiments were performed as shown in Fig. 9(a). The ATI Nano 17 force sensor was installed inside another 3-D-printed ball with a diameter of 40 mm. The ball was again placed toward each finger to measure the pinching force generated by that finger. The results of the pinching forces of Gripper-A are plotted in Fig. 9(b) when the actuation force increases from 50 to 200 N. The pinching experiments were not successful for Gripper-B because one finger generated higher forces and it always pushed the ball out, as in Fig. 9(c).

The pinching forces in Fig. 9(b) are relatively small, mainly because the crank's moment-arm length in Fig. 7(c) is about one-tenth of the finger length. Furthermore, part of the input force is used to deform the CDM. The CDM inherently acts as a reservoir of energy, whereas a KDM needs to install additional springs for this feature. When the scales of the gripper and the CDM are increased, the CDM might absorb a bigger portion of the input energy. A CDM is probably more suitable for light loads with the input force from zero to a few hundred newtons.

The pull-out experiments were performed, as shown in Fig. 10(a). The grippers were actuated by hanging weights to the input backbone. The total input forces varied from 12 to 102 N. A baseball was grasped and pulled out. The pull-out motion was realized by a lead screw and the pull-out force was measured using a force gauge (HF-200 from Yueqing Aliyiqi Instrument Co. China with a built-in function for peak force measurement and a range of ± 200 N).

The pull-out forces are plotted in Fig. 10(b). From the grasping experiments, it is known that Gripper-B would push the grasped baseball aside. This outcome actually helped Gripper-B to achieve a higher pull-out force under the same input. If the pull-out direction leans toward the weaker fingers of Gripper-B, the pull-out forces might be reduced.

V. Conclusion

This paper has proposed to categorize differential mechanisms into KDMs and CDMs. KDMs generate differential outputs via motions of the kinematic pairs, while CDMs utilize the redistributions and/or deformations of their own materials and structures to generate differential outputs. The IFToMM terminology could be expanded to cover the CDMs.

A planar CDM and a spatial CDM is then introduced. Kinetostatic analyses and experimental characterizations are carried out to reveal their force transmission properties. The equivalency between the planar CDM and two existing KDMs is indicated. On the other hand, the spatial CDM resolves one input into three outputs in an inherently isotropic way. This feature was demonstrated via a series of experiments performed on two three-fingered grippers driven by one spatial CDM and two serially connected planar CDMs.

Due to the inherent compliance and deforming properties, the CDMs might not be ideal for large outputs. However, the simple construction and cheap fabrication of the CDMs could indeed be advantageous. Following the analyses and experiments presented in this paper, hopefully one could design other CDMs with various force transmission responses and properties to realize compact, affordable, and adaptive mechanical systems.

References

[1] IFToMM, "Standardization of terminology," in *IFToMM Dictionaries*, International Federation for the Promotion of Mechanism and Machine Science, 2007.

[2] L. Birglen and C. M. Gosselin, "Force analysis of connected differential mechanisms: Application to grasping," *Int. J. Robot. Res.*, vol. 25, no. 10, pp. 1033–1046, Oct. 2006.

[3] C. Gosselin, F. Pelletier, and T. Laliberté, "An anthropomorphic underactuated robotic hand with 15 DoFs and a single actuator," in *Proc. IEEE Int. Conf. Robot. Autom.*, Pasadena, CA, USA, 2008, pp. 749–754.

[4] M. Baril, T. Laliberté, C. Gosselin, and F. Routhier, "On the design of a mechanically programmable underactuated anthropomorphic prosthetic gripper," *J. Mech. Des.*, vol. 135, no. 12, p. 121008–1, Oct. 2013.

[5] J. T. Belter and A. M. Dollar, "Novel differential mechanism enabling two DOF from a single actuator: Application to a prosthetic hand," in *Proc. IEEE Int. Conf. Rehabil. Robot.*, Seattle, WA, USA, 2013, pp. 1–6.

[6] N. Fukaya, S. Toyama, T. Asfour, and R. Dillmann, "Design of the TUAT/Karlsruhe humanoid hand," in *Proc. IEEE/RSJ Int. Conf. Intell. Robots Syst.*, Takamatsu, Japan, 2000, pp. 1754–1759.

[7] Y. Kamikawa and T. Maeno, "Underactuated five-finger prosthetic hand inspired by grasping force distribution of humans," in *Proc. IEEE/RSJ Int. Conf. Intell. Robots Syst.*, Nice, France, 2008, pp. 717–722.

[8] L. Birglen, T. Laliberté, and C. Gosselin, "Design and control of the Laval underactuated hands," in *Underactuated Robotic Hands*, vol. 40. Berlin, Germany: Springer, 2008, pp. 171–207.

[9] V. Bégoc, S. Krut, E. Dombre, C. Durand, and F. Pierrot, "Mechanical design of a new pneumatically driven underactuated hand," in *Proc. IEEE Int. Conf. Robot. Autom.*, Roma, Italy, 2007, pp. 927–933.

[10] C. Y. Brown and H. H. Asada, "Inter-finger coordination and postural synergies in robot hands via mechanical implementation of principal components analysis," in *Proc. IEEE/RSJ Int. Conf. Intell. Robots Syst.*, San Diego, CA, USA, 2007, pp. 2877–2882.

[11] W. Chen, C. Xiong, and S. Yue, "Mechanical implementation of kinematic synergy for continual grasping generation of anthropomorphic hand," *IEEE/ASME Trans. Mechatronics*, vol. 20, no. 3, pp. 1249–1263, May 2015.

[12] S. Li, X. Sheng, H. Liu, and X. Zhu, "Design of a myoelectric prosthetic hand implementing postural synergy mechanically," *Ind. Robot: An Int. J.*, vol. 41, no. 5, pp. 447–455, 2014.

[13] K. Xu, J. Zhao, Y. Du, X. Sheng, and X. Zhu, "Design and postural synergy synthesis of a prosthetic hand for a manipulation task," in *Proc. IEEE/ASME Int. Conf. Adv. Intell. Mechatron.*, Wollongong, NSW, Australia, 2013, pp. 56–62.

[14] K. Xu, H. Liu, Y. Du, and X. Zhu, "Design of an underactuated anthropomorphic hand with mechanically implemented postural synergies," *Adv. Robot.*, vol. 28, no. 21, pp. 1459–1474, Nov. 2014.

[15] L. Birglen and C. M. Gosselin, "Kinetostatic analysis of underactuated fingers," *IEEE Trans. Robot. Autom.*, vol. 20, no. 2, pp. 211–221, Apr. 2004.

[16] S. Krut, "A force-isotropic underactuated finger," in *Proc. IEEE Int. Conf. Robot. Autom.*, Barcelona, Spain, 2005, pp. 2314–2319.

[17] M. C. Carrozza, G. Cappiello, S. Micera, B. B. Edin, L. Beccai, and C. Cipriani, "Design of a cybernetic hand for perception and action," *Biol. Cybern.*, vol. 95, no. 6, pp. 629–644, 2006.

[18] L. Zollo, S. Roccella, E. Guglielmelli, M. C. Carrozza, and P. Dario, "Biomechatronic design and control of an anthropomorphic artificial hand for prosthetic and robotic applications," *IEEE/ASME Trans. Mechatron.*, vol. 12, no. 4, pp. 418–429, Aug. 2007.

[19] S. A. Dalley, T. E. Wiste, T. J. Withrow, and M. Goldfarb, "Design of a multifunctional anthropomorphic prosthetic hand with extrinsic actuation," *IEEE/ASME Trans. Mechatron.*, vol. 14, no. 6, pp. 699–706, Nov. 2009.

[20] W. Townsend, "The BarrettHand Grasper—Programmably flexible part handling and assembly," *Ind. Robot: Int. J.*, vol. 27, no. 3, pp. 181–188, 2000.

[21] A. Pringle, "Artificial hand," U.S. Patent 1 324 564, 1919.

[22] N. Decheva, W. L. Cleghorn, and S. Naumann, "Multiple finger, passive adaptive grasp prosthetic hand," *Mech. Mach. Theory*, vol. 36, no. 10, pp. 1157–1173, Oct. 2001.

[23] B. Massa, S. Roccella, M. C. Carrozza, and P. Dario, "Design and development of an underactuated prosthetic hand," in *Proc. IEEE Int. Conf. Robot. Autom.*, Washington, DC, USA, 2002, pp. 3374–3379.

[24] M. C. Carrozza *et al.*, "A cosmetic prosthetic hand with tendon driven under-actuated mechanism and compliant joints: Ongoing research and preliminary results," in *Proc. IEEE Int. Conf. Robot. Autom.*, Barcelona, Spain, 2005, pp. 2661–2666.

[25] A. M. Dollar and R. D. Howe, "The highly adaptive SDM hand: design and performance evaluation," *Int. J. Robot. Res.*, vol. 29, no. 5, pp. 585–597, Apr. 2010.

[26] K. Xu, H. Liu, Z. Liu, Y. Du, and X. Zhu, "A single-actuator prosthetic hand using a continuum differential mechanism," in *Proc. IEEE Int. Conf. Robot. Autom.*, Seattle, WA, USA, 2015, pp. 6457–6462.

[27] X. Wang and J. K. Mills, "Dynamic modeling of a flexible-link planar parallel platform using a substructuring approach," *Mech. Mach. Theory*, vol. 41, no. 6, pp. 671–687, Jun. 2006.

[28] K. Xu and N. Simaan, "An investigation of the intrinsic force sensing capabilities of continuum robots," *IEEE Trans. Robot.*, vol. 24, no. 3, pp. 576–587, Jun. 2008.

[29] K. Xu and N. Simaan, "Analytic formulation for the kinematics, statics and shape restoration of multibackbone continuum robots via elliptic integrals," *J. Mech. Robot.*, vol. 2, no. 011006, pp. 1–13, Feb. 2010.

[30] G. Carbone, *Grasping in Robotics*, vol. 10. London, U.K.: Springer, 2013.